

Origin of the Verwey transition in magnetite: Group theory, electronic structure and lattice dynamics study

Przemysław Piekarz, Krzysztof Parlinski, and Andrzej M. Oleś

Institute of Nuclear Physics, Polish Academy of Sciences, Radzikowskiego 152, PL-31342 Kraków, Poland

(Dated: February 2, 2008)

The Verwey phase transition in magnetite has been analyzed using the group theory methods. It is found that two order parameters with the symmetries X_3 and Δ_5 induce the structural transformation from the high-temperature cubic to the low-temperature monoclinic phase. The coupling between the order parameters is described by the Landau free energy functional. The electronic and crystal structure for the cubic and monoclinic phases were optimized using the *ab initio* density functional method. The electronic structure calculations were performed within the generalized gradient approximation including the on-site interactions between 3d electrons at iron ions — the Coulomb element U and Hund's exchange J . Only when these local interactions are taken into account, the phonon dispersion curves, obtained by the direct method for the cubic phase, reproduce the experimental data. It is shown that the interplay of local electron interactions and the coupling to the lattice drives the phonon order parameters and is responsible for the opening of the gap at the Fermi energy. Thus, it is found that the metal-insulator transition in magnetite is promoted by local electron interactions, which significantly amplify the electron-phonon interaction and stabilize weak charge order coexisting with orbital order of the occupied t_{2g} states at Fe ions. This provides a scenario to understand the fundamental problem of the origin of the Verwey transition in magnetite.

PACS numbers: 71.30.+h, 71.38.-k, 64.70.Kb, 75.50.Gg

I. INTRODUCTION

For many decades, magnetite — the oldest known magnetic material — has been a fascinating subject of extensive research. Besides its distinct magnetic properties, the main interest was focused on the mechanism and physical consequences of the first-order phase transition at $T_V = 122$ K, called the Verwey transition (VT), in which conductivity changes by about two orders of magnitude.¹ For a long time it has been considered as an example of charge localization driven by metal-insulator transition,² in which ionic interactions determine the electronic properties.³ Only in the last decade the progress in experimental and theoretical techniques, as well as improved quality of samples, allowed one for a deeper insight into the nature of this transition.⁴ Recent studies demonstrated that the VT is a cooperative phenomenon, in which an interplay between lattice, charge, and orbital degrees of freedom plays a decisive role. In this context, magnetite remains to be one of the most interesting materials among transition metal oxides.⁵

At room temperature, magnetite (Fe_3O_4) crystallizes in the inverse spinel cubic structure with Fe ions occupying the tetrahedral A sites and octahedral B sites, as shown in Fig. 1. The ionic structure of magnetite in the inverse spinel phase is $\text{Fe}^{3+}(A)\text{Fe}^{2.5+}(B)\text{Fe}^{2.5+}(B)\text{O}_4^{2-}$. Below the Néel temperature $T_N = 851$ K, magnetic moments at Fe ions are aligned antiparallelly between A and B sites, which results in the ferrimagnetic state. Verwey proposed that the metal-insulator transition is caused by the charge order (CO) of Fe^{2+} and Fe^{3+} ions at the B sites, in planes perpendicular to the c axis.² The structural analysis, however, revealed the crystal distortion, which is incompatible with the Verwey model. In particular,

the observation of half-integer reflections at $(h, k, l + \frac{1}{2})$ points indicated the doubling of the unit cell along the c axis.⁶ Further diffraction studies by neutron,^{7,8} x-ray,⁹ and electron¹⁰ scattering established the monoclinic symmetry of the low temperature (LT) phase realized below T_V . Indeed, the number of inequivalent A and B atomic positions found by nuclear magnetic resonance (NMR) for the phase below the VT^{11,12,13} agrees with the monoclinic structure.

The models to describe the CO in magnetite, consist-

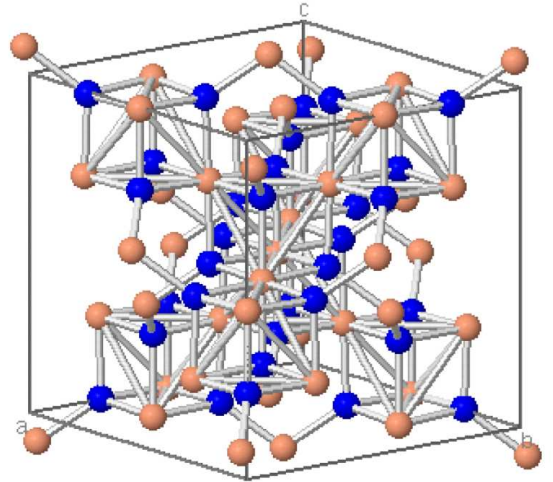


FIG. 1: (Color online) The crystal structure of magnetite in the cubic $Fd\bar{3}m$ symmetry. Iron and oxygen ions are represented by grey and dark (orange and blue) balls. $\text{Fe}(B)$ ions have six O neighbors, while each O ion has three $\text{Fe}(B)$ and one $\text{Fe}(A)$ neighbor.

tent with the LT phase of Fe_3O_4 , have been proposed in many studies.^{10,11,12,13} High-resolution neutron and x-ray scattering measurements^{14,15} revealed the distribution of Fe-O bond distances in the BO_6 octahedra (between 1.96 and 2.11 Å), being the indication of charge disproportionation on Fe(*B*) ions. The CO proposed by Attfield *et al.*^{14,15} is considerably more complex than the Verwey model¹ itself, and consists of four different *B* sites in a unit cell, with approximately two valence states: $\text{Fe}^{+2.4}$ and $\text{Fe}^{+2.6}$. Providing a convincing evidence in favor of such a state has been a challenge for several direct probing methods including the resonant x-ray scattering. Despite preliminary negative results,^{16,17} the evidence that the CO is indeed fractional has accumulated recently.^{18,19,20,21} It is clear from the character of the observed CO that a simple ionic mechanism suggested early on by Anderson³ cannot explain the VT.

The electronic structure of magnetite was studied by the density functional theory (DFT) calculations in the local spin density approximation (LSDA).²² This approach is based on the local density approximation (LDA) and provides a basic description of the electronic structure and magnetic properties of Fe_3O_4 in the cubic phase above T_V .^{22,23,24} The CO instability induced by local on-site and intersite Coulomb interactions was studied in the cubic symmetry within the LSDA+*U* method.^{25,26} For a distorted (orthorhombic) symmetry, the self-interaction correction²⁷ approach was used, and it has been shown that the CO proposed by Verwey does not appear in the ground state of magnetite. The calculations for the experimentally observed monoclinic structure, performed within the LSDA+*U* (see Refs. 28,29) and generalized gradient approximation (GGA) with local Coulomb interaction *U* (GGA+*U*, see, e.g. Ref. 30) approaches proved the existence of fractional charge disproportionation in fair agreement with the experimental analysis.¹⁴ In addition, these studies revealed the presence of the orbital order (OO) of the occupied t_{2g} states at *B*-sites,^{29,30} in agreement with recent experiments performed on thin films of Fe_3O_4 .³¹ The obtained magnitude of the insulating gap agrees well with the photoemission data below T_V .^{32,33,34} On the contrary, in absence of electron interactions (for $U = 0$) the electronic state remains metallic even in the distorted structure, showing the essential role played by local electron interactions in the VT. These *ab initio* calculations demonstrate also that the microscopic understanding of the VT requires to involve lattice distortions and electron-phonon (EP) interaction.

The experimental evidence that phonons participate in the mechanism of the VT is very convincing. The structural analysis showed that the LT phase results from the condensation of modes at three reciprocal lattice points: $\mathbf{k}_\Gamma = (0, 0, 0)$, $\mathbf{k}_\Delta = (0, 0, \frac{1}{2})$, and $\mathbf{k}_X = (0, 0, 1)$,^{8,15} in units of $\frac{2\pi}{a}$, where *a* is lattice constant of the cubic structure. The pronounced softening of the c_{44} elastic constant,³⁵ observed from room temperature down to T_V , has been explained by the coupling between the

shear mode and the charge-density T_{2g} order parameter (OP) at the Γ point.³⁶ The decrease of c_{44} is associated with the softening of the surface Rayleigh mode observed by the Brillouin scattering.³⁷ In the bulk, no phonon softening has been observed,³⁸ however, critical fluctuations revealed by neutron scattering strongly indicate the existence of phonon precursor effects which drive the structural deformation. First, the spotlike diffuse signal was observed at the reciprocal space point $\mathbf{k}_\Delta = (4, 0, \frac{1}{2})$.³⁹ Yamada proposed that the VT results from the condensation of a coupled charge density-phonon mode with Δ_5 symmetry, explaining the intensities of neutron signal and \mathbf{k}_Δ Bragg reflections.⁴⁰ Second, a new type of planar diffuse scattering was found over a broad region of the reciprocal space at high temperature $T_V < T < T_V + 100$ K.^{41,42} The signal around the Γ and equivalent points was interpreted as the Huang scattering due to the local strain field, and was studied in the molecular polaron model.^{43,44} The analysis of intensities at \mathbf{k}_X points led to the conclusion that transverse phonons with the X_3 symmetry dominate in neutron scattering.⁴⁵ The phonon mechanism is further supported by oxygen isotope effect,⁴⁶ Raman,^{47,48,49} the extended x-ray absorption fine structure (EXAFS),⁵⁰ and by nuclear inelastic scattering (NIS) measurements.⁵¹

The idea that both Coulomb interactions and the EP coupling are responsible for the VT was first explored by Ihle and Lorentz.⁵² They combined the tight-binding model introduced by Cullen and Callen⁵³ with the Yamada model.⁴⁰ In their approach, the CO below T_V is driven by the intersite electrostatic interactions and the condensation of the Δ_5 phonon.⁵⁴ Above T_V , the model explains the short-range polaronic order and provides a good description of the electric conductivity.⁵⁵ Indeed, the polaronic character of charge carriers has been observed in the optical conductivity^{48,56} and in photoemission studies.³⁴ The cooperative mechanism of the VT was next studied also in the Peierls-Hubbard model,⁵⁷ where strong on-site interaction induces the OO and lattice distortion. Since the active electrons on Fe^{+2} ions occupy partly filled degenerate t_{2g} states, the EP coupling could be further enhanced by the Jahn-Teller effect. This mechanism was confirmed by the dynamical mean-field theory (DMFT) combined with the DFT in the GGA+DMFT method,⁵⁸ and by GGA+*U* calculations,⁵⁹ which showed that the local Jahn-Teller distortions modify the electronic structure lead indeed to opening of the insulating gap.

In the previous paper,⁶⁰ we reported the phonon spectrum obtained using the direct method,⁶¹ and analyzed the EP interactions in presence of local Coulomb interaction *U*. We have found that two phonon modes with X_3 and Δ_5 symmetry, which significantly distort the *B*-site octahedra, couple strongly to t_{2g} electronic states. The X_3 phonon opens the gap at the Fermi energy, and drives the metal-insulator transition. Using the group theory, we proved that these two modes are primary order parameters describing the structural phase transition.

The purpose of the present paper is to focus on the details of the group theory analysis of the phase transformation in the magnetite, from the cubic $Fd\bar{3}m$ to monoclinic $P2/c$ symmetry, and to relate it to the simultaneous changes in the electronic structure and lattice dynamics. A full list of relevant OPs will be presented and their couplings will be discussed on the basis of Landau free energy. In the second part of the paper we focus on the results of structural optimization and lattice dynamics calculations in presence of local electron interactions, and demonstrate that the phase transformation in the VT involves the EP interaction.

The paper is organized as follows. In Sec. II the group theory analysis of the VT is presented. Sec. III is devoted to the electronic structure calculation, where we first present the method used (Sec. III A), and next analyze the optimized crystal structures (Sec. III B). In Sec. IV we describe lattice dynamics and classify the obtained modes for the magnetite using the irreducible representations of the cubic group. These results serve as a basis to discuss the EP interactions and their effect on the electronic structure in Sec. V. We show a strong coupling between the electronic properties and lattice dynamics, and in this context discuss the mechanism of the VT in Sec. VI. The paper is concluded in Sec. VII, where we provide a coherent view on the VT in magnetite and summarize the presented results.

II. GROUP THEORY ANALYSIS

A. Primary and secondary order parameters

In a structural phase transition the symmetry is lowered from the high-symmetry phase, usually realized at high temperature, to the low-symmetry one, stable at low temperature. The Verwey transition in magnetite belongs to this class of phase transitions, so we consider first the Landau free energy functional to characterize the OPs responsible for the observed lowering of symmetry. In the Landau-type phase transition the space group \mathcal{L} of the low-symmetry phase is a subgroup of the space group \mathcal{H} of the high-symmetry phase, i.e., $\mathcal{L} \subset \mathcal{H}$. There exists often one irreducible representation (IR) of \mathcal{H} , which reduces the symmetry to \mathcal{L} . This allows one to identify an OP as a vector in an IR space, $\Gamma_{\mathbf{k},j}(\eta_i)$, where \mathbf{k} is a wave vector of the irreducible star, j is the index of ray representation, and η_i are the components of the OP.⁶² The OP which defines the transition and determines the symmetry of the low-symmetry phase is called a *primary* OP, and the symmetry reduction diagram for it can be written as follows

$$\mathcal{H} \rightarrow [\Gamma_{\mathbf{k},j}(\eta_i)] \rightarrow \mathcal{L}. \quad (1)$$

In contrast, a *secondary* OP $\gamma_{\mathbf{k},j}(\eta_i)$ is associated with an IR which reduces the symmetry of the high-symmetry space group to an intermediate space group \mathcal{I} , such that

\mathcal{I} becomes a subgroup to \mathcal{H} , and a supergroup for \mathcal{L} , i.e., $\mathcal{L} \subset \mathcal{I} \subset \mathcal{H}$.⁶³ Thus, the symmetry reduction diagram has the form

$$\mathcal{H} \rightarrow [\gamma_{\mathbf{k},j}(\eta_i)] \rightarrow \mathcal{I}. \quad (2)$$

The secondary OP appears in the Landau free energy expansion always in a term which provides a linear coupling of this secondary OP to a quadratic (or higher power) expression in the relevant primary OP. At the phase transition the primary OP starts to develop, while the secondary OPs also become finite because of their coupling to the primary OP.

In principle a phase transition could be induced by two or more primary OPs, and they can be coupled to the secondary ones. Thus, in general N primary OPs, $\text{IR}_1, \text{IR}_2, \dots, \text{IR}_N$, reduce the high-symmetry space group \mathcal{H} into $\mathcal{L}_1, \mathcal{L}_2, \dots, \mathcal{L}_N$ low-symmetry space groups, respectively,

$$\begin{aligned} \mathcal{H} &\rightarrow [\Gamma_{\mathbf{k}_1,j_1}(\eta_i)] \rightarrow \mathcal{L}_1, \\ \mathcal{H} &\rightarrow [\Gamma_{\mathbf{k}_2,j_2}(\eta_i)] \rightarrow \mathcal{L}_2, \\ &\dots \\ \mathcal{H} &\rightarrow [\Gamma_{\mathbf{k}_N,j_N}(\eta_i)] \rightarrow \mathcal{L}_N. \end{aligned} \quad (3)$$

Due to a non-linear coupling between the primary OPs, the final low-symmetry space group \mathcal{L} is an intersection of all low-symmetry space groups

$$\mathcal{L} = \mathcal{L}_1 \cap \mathcal{L}_2 \cap \dots \mathcal{L}_N. \quad (4)$$

Thus, the low-symmetry space group \mathcal{L} consists of those symmetry elements which are present in *all subgroups* $\mathcal{L}_1, \mathcal{L}_2, \dots, \mathcal{L}_N$. The secondary OPs are associated with IRs which reduce the symmetry of the high-symmetry space group to intermediate space groups \mathcal{I}_m , such that

TABLE I: List of OPs from the parent space group $Fd\bar{3}m$ (No=227) and basis $\{(1,0,0), (0,1,0), (0,0,1)\}$ to the monoclinic phase $P2/c$ (No=13, unique axis b , choice 1), basis $\{(\frac{1}{2}, -\frac{1}{2}, 0), (\frac{1}{2}, \frac{1}{2}, 0), (0,0,2)\}$ and origin $(\frac{1}{4}, 0, \frac{1}{4})$ relative to the original face center cubic lattice. Size is the ratio of the volumes of primitive low-symmetry to high-symmetry unit cells. The direction of the IR vector given in the last column indicates its nonvanishing components as well as the relations between the components of the OPs.

IR	size	subgroup	No	IR vector
Γ_1^+	1	$Fd\bar{3}m$	227	(a)
Γ_3^+	1	$I4_1/amd$	141	(b, 0)
Γ_4^+	1	$C2/m$	12	(c, c, 0)
Γ_5^+	1	$Imma$	74	(d, 0, 0)
Γ_5^+	1	$C2/m$	12	(d, e, -e)
X_1	2	$Pmma$	51	(f, 0, 0, 0, 0, 0)
X_3	2	$Pmna$	53	(g, 0, 0, 0, 0, 0)
Δ_2	4	$Pcca$	54	(0, 0, 0, 0, h, $-\frac{1}{\mu}h$)
Δ_4	4	$Pcca$	54	(0, 0, 0, 0, p, μp)
Δ_5	4	$Pbcm$	57	(0, 0, 0, 0, 0, 0, 0, q, $-\mu q, -\mu q, -q$)

TABLE II: Subgroup relationships and the IRs creating the symmetry reduction from space group \mathcal{H} to a given \mathcal{I} and \mathcal{L} space groups, respectively. In brackets are the sizes of primitive unit cells.

Subgroup relationships	Group No's	Secondary OP	Primary OP
$Fd\bar{3}m(1) \supset I4_1amd(1) \supset Pmma(2) \supset Pbcm(4)$	227, 141, 51, 57	Γ_3^+, X_1	Δ_5
$Fd\bar{3}m(1) \supset Imma(1) \supset Pmma(2) \supset Pcca(4)$	227, 74, 51, 54	Γ_5^+, X_1	Δ_2, Δ_4
$Fd\bar{3}m(1) \supset I4_1amd(1) \supset Pmna(2)$	227, 141, 53	Γ_3^+	X_3
$Fd\bar{3}m(1) \supset Imma(1) \supset Pmna(2)$	227, 74, 53	$\Gamma_5^+ (d, 0, 0)$	X_3
$Fd\bar{3}m(1) \supset Imma(1) \supset C2/m(1)$	227, 74, 12	$\Gamma_5^+ (d, 0, 0)$	$\Gamma_5^+ (d, e, -e)$

TABLE III: Intersections of subgroups listed in Table I which lead to low-symmetry space group $P2/c$. In all cases the size is equal 4, the basis vectors are $\{(\frac{1}{2}, -\frac{1}{2}, 0), (\frac{1}{2}, \frac{1}{2}, 0), (0, 0, 2)\}$ and the origin is $(\frac{1}{4}, 0, \frac{1}{4})$.

No	IRs	subgroups giving $P2/c$	subgroup No's
1	X_3, Δ_5	$Pmna \cap Pbcm$	$(53, 57) = 13$
2	X_3, Δ_2	$Pmna \cap Pcca$	$(53, 54) = 13$
3	X_3, Δ_4	$Pmna \cap Pcca$	$(53, 54) = 13$
4	$X_3, \Delta_5, \Gamma_5^+$	$Pmna \cap Pbcm \cap C2/m$	$(53, 57, 12) = 13$
5	$X_3, \Delta_2, \Gamma_5^+$	$Pmna \cap Pcca \cap C2/m$	$(53, 54, 12) = 13$
6	$X_3, \Delta_4, \Gamma_5^+$	$Pmna \cap Pcca \cap C2/m$	$(53, 54, 12) = 13$
7	X_3, Δ_5, Δ_2	$Pmna \cap Pbcm \cap Pcca$	$(53, 57, 54) = 13$
8	X_3, Δ_5, Δ_4	$Pmna \cap Pbcm \cap Pcca$	$(53, 57, 54) = 13$
9	X_3, Δ_2, Δ_4	$Pmna \cap Pcca \cap Pcca$	$(53, 54, 54) = 13$
10	$X_3, \Delta_5, \Delta_2, \Gamma_5^+$	$Pmna \cap Pbcm \cap Pcca \cap C2/m$	$(53, 57, 54, 12) = 13$
11	$X_3, \Delta_5, \Delta_4, \Gamma_5^+$	$Pmna \cap Pbcm \cap Pcca \cap C2/m$	$(53, 57, 54, 12) = 13$
12	$X_3, \Delta_2, \Delta_4, \Gamma_5^+$	$Pmna \cap Pcca \cap Pcca \cap C2/m$	$(53, 54, 54, 12) = 13$
13	$X_3, \Delta_5, \Delta_2, \Delta_4$	$Pmna \cap Pbcm \cap Pcca \cap Pcca$	$(53, 57, 54, 54) = 13$
14	$X_3, \Delta_5, \Delta_2, \Delta_4, \Gamma_5^+$	$Pmna \cap Pbcm \cap Pcca \cap Pcca \cap C2/m$	$(53, 57, 54, 54, 12) = 13$

$\mathcal{L}_n \subset \mathcal{I}_m \subset \mathcal{H}$, where $n = 1, 2, \dots, N$ and m should be found by inspection the group-subgroup relationships

$$\begin{aligned}
 \mathcal{H} &\rightarrow [\gamma_{\mathbf{k}_1, j_1}(\eta_i)] \rightarrow \mathcal{I}_1, \\
 \mathcal{H} &\rightarrow [\gamma_{\mathbf{k}_2, j_2}(\eta_i)] \rightarrow \mathcal{I}_2, \\
 &\dots \\
 \mathcal{H} &\rightarrow [\gamma_{\mathbf{k}_m, j_m}(\eta_i)] \rightarrow \mathcal{I}_m.
 \end{aligned} \tag{5}$$

For instance, a symmetry reduction in shape memory alloy NiTi, associated with the symmetry change $Pm\bar{3}m \rightarrow P2_1/m$, is a phase transition which involves two primary OPs.^{64,65} As we demonstrate in this Section, the symmetry reduction realized in the VT of magnetite requires also multiple primary and secondary OPs.

The high-symmetry space group of Fe_3O_4 above T_V is $\mathcal{H} = Fd\bar{3}m$ (Fig. 1). The low-symmetry phase \mathcal{L} was identified as the monoclinic Cc symmetry^{7,8,9,10} with a unit cell of approximate size $\sqrt{2}a \times \sqrt{2}a \times 2a$. As argued by Iizumi *et al.*,⁸ a smaller cell $a/\sqrt{2} \times a/\sqrt{2} \times 2a$ with the $Pmca$ symmetry can be used for refinement almost all Bragg reflections. In Ref. 15, the monoclinic symmetry $P2/c$ with orthorhombic constraints was used in the refinement procedure. This symmetry describes all Bragg peaks except for three very weak reflections arising from atomic displacements smaller than 0.01 \AA .¹⁵ Indeed, the unit cell used in the refinement procedure takes into account all atomic displacements coming from \mathbf{k}_Γ , \mathbf{k}_Δ , and \mathbf{k}_X points. Therefore, the $P2/c$ symmetry explains

majority of physical properties connected with the VT.

Here, we present a detailed group theory analysis of the structural transition for $\mathcal{L} = P2/c$ (No=13), with basis $\{(\frac{1}{2}, -\frac{1}{2}, 0), (\frac{1}{2}, \frac{1}{2}, 0), (0, 0, 2)\}$ and the origin $(\frac{1}{4}, 0, \frac{1}{4})$ relative to the original face center cubic lattice. Using the COPL and ISOTROPY computer codes^{66,67} we obtained the lists of possible intermediate $\{\mathcal{I}_m\}$ and low-symmetry $\{\mathcal{L}_n\}$ space groups, and show them in Table I. The space groups, which have been found, are reduced by IRs from the high-symmetry space group $\mathcal{H} = Fd\bar{3}m$. As is clearly seen, there is no IR which reduces $Fd\bar{3}m$ to low-symmetry $\mathcal{L} = P2/c$. This means that the phase transition in Fe_3O_4 is driven by *at least* two primary OPs. A closer inspection of space group-subgroup relationships, partly shown in Table II, leads us to the conclusion that in principle there are five primary OPs: X_3 , Δ_2 , Δ_4 , and Δ_5 , and Γ_5^+ (T_{2g}) within direction $(d, e, -e)$. Indeed, the intersection of space groups being the result of symmetry reduction of $Fd\bar{3}m$ by the above mentioned IRs provides the observed low-symmetry space group $P2/c$, Table III.

In the the simplest case, the $P2/c$ symmetry can be induced by two OPs. Taking the X_3 and Δ_5 symmetries, the reduction diagrams can be written

$$\begin{aligned}
 Fd\bar{3}m &\rightarrow [X_3, \mathbf{k} = (0, 0, 1)] \rightarrow Pmna, \\
 Fd\bar{3}m &\rightarrow \left[\Delta_5, \mathbf{k} = \left(0, 0, \frac{1}{2}\right) \right] \rightarrow Pbcm.
 \end{aligned} \tag{6}$$

Now, if we take common symmetry elements (an inter-

section) of these two groups, we get

$$Pmna \cap Pbcm = P2/c, \quad (7)$$

so the low-symmetry space group has indeed $P2/c$ symmetry. The remaining IRs involved in the phase transition $\Gamma_1^+ (A_{1g})$, $\Gamma_3^+ (E_g)$, $\Gamma_4^+ (T_{1g})$, $\Gamma_5^+ (T_{2g})$ within direction $(d, 0, 0)$, and X_1 are the secondary OPs. On the one hand, it is evident that Γ_5^+ can be either primary or secondary OP. If only one component d is nonzero it has a secondary character and its reduction diagram reads

$$Fd\bar{3}m \rightarrow [\Gamma_5^+(d, 0, 0), \mathbf{k} = (0, 0, 0)] \rightarrow Imma. \quad (8)$$

The resulting group fulfills the following subgroup relationship

$$Fd\bar{3}m \supset Imma \supset Pmna, \quad (9)$$

so Γ_5^+ as the secondary OP couples to the primary OP X_3 . On the other hand, if all three components of Γ_5^+ are nonzero, it has primary character with the reduction diagram

$$Fd\bar{3}m \rightarrow [\Gamma_5^+(d, e, -e), \mathbf{k} = (0, 0, 0)] \rightarrow C2/m. \quad (10)$$

Because of the following relationship

$$Fd\bar{3}m \supset Imma \supset C2/m, \quad (11)$$

$\Gamma_5^+(d, 0, 0)$ is the secondary parameter of the $\Gamma_5^+(d, e, -e)$ OP. In what follows, we shall use the point group notation of the IRs at the Γ point. This notation is usually used in experimental works on phonon spectroscopy.

As is clear from this analysis, the X_3 OP plays an exceptional role among other symmetries, being present in all intersections listed in Table III. So one recognizes that this OP is essential to generate the LT monoclinic phase and it confirms its precursor behavior found in the diffuse scattering study. As we showed by the *ab initio* calculations, this mode strongly couples to electrons and induces the metal-insulator transition.⁶⁰

At the \mathbf{k}_Δ point, there are three possible OPs: Δ_2 , Δ_4 , and Δ_5 . In principle, by coupling to X_3 either of these modes can induce $P2/c$ symmetry, but one of them, Δ_5 , has a strong support from the experiment. Originally proposed by Yamada⁴⁰ — this mode was found to be the main component of lattice distortion in critical neutron scattering.³⁹ Neutron studies by Iizumi *et al.*⁸ confirmed the Δ_5 pattern of displacements, which gives rise to \mathbf{k}_Δ Bragg peaks. The EP interaction for the Δ_5 mode was studied within the model of Ihle and Lorenz.⁵² At the Γ point there could be only one primary OP with T_{2g} symmetry. It is related with the softening of the elastic constant c_{44} . Notice that in the cubic system one has $c_{44} = c_{55} = c_{66}$, and therefore one is unable to differentiate between the secondary $(d, 0, 0)$ or primary $(d, e, -e)$

OP characters. A strong EP interaction for the T_{2g} mode was found by the Raman experiment⁴⁹ and in neutron diffuse measurements.⁴⁴ Taking into account that only t_{2g} electronic states are present near the Fermi level, a strong coupling to phonons with the same symmetry is not surprising. Altogether, from experimental observations and from *ab initio* calculations, presented in detail in the next Sections, we have strong evidence for the following three primary OPs being involved in the phase transition: X_3 , Δ_5 , and T_{2g} .

To appreciate fully the complexity of the resulting LT phase, we emphasize that although the LT symmetry is uniquely determined by the primary OPs, the exact atomic positions result from all lattice distortions, associated also with secondary OPs. The X_1 type distortion was reported in x-ray⁶⁸ and in neutron⁸ diffraction. The mechanism stabilizing the incommensurate mode Δ_5 at wavevector \mathbf{k}_Δ by simultaneous condensation with the X_1 phonon was discussed by Iizumi.⁶⁹ The X_1 mode induces the longitudinal displacements with $\lambda = a$ observed in the monoclinic structure.¹⁵ There are a few secondary OPs at the zone center, and they are likely to participate in the LT structure as well.^{8,15} For example, the anomaly related to the observed changes in frequency and linewidth at the phase transition was found for the highest Raman A_{1g} mode.⁴⁸

B. Free energy functional

Knowing the primary and secondary OPs and their IRs, one can construct the invariant quantities which do not change under symmetry group transformations, and next expand the free energy \mathcal{F} into a series of the components which involve different OPs.⁶⁷ Each component is a linear combination of its electronic and phononic parts, which represent the electronic density and atomic displacement contributions, respectively. For instance, the component of X_3 can be written in the form which includes its electronic and phononic contribution: $g = g_{el} + g_{ph}$. Note that in the present case of active t_{2g} degrees of freedom of $3d$ electrons at iron ions, the electronic part g_{el} may as well involve the orbital occupations.

We limit the expansion of the free energy \mathcal{F} to the 4-th order terms, with the exception of two primary OPs X_3 and Δ_5 , for which we include also terms of 6-th order as they are typical for the discontinuous (first-order) phase transitions. A complete expansion gives too lengthy expression to be reproduced here, so we leave in the expansion only components of OPs required by symmetry as shown in Table I, and write down only the potentially nonvanishing terms. Each term of the series must be multiplied by factors depending on thermodynamical parameters, however, we shall not discuss this aspect here. The free energy reads

$$\begin{aligned}
\mathcal{F} = & (g^2 + q^2 + g^4 + q^4 + g^2q^2 + g^6 + g^4q^2 + g^2q^4 + q^6) + (p^2 + h^2 + g^2p^2 + g^2h^2 + q^2p^2 + q^2h^2 + p^2h^2 + gq(h+p)) \\
& + (f^2 + fq^2 + fp^2 + fh^2 + fph + f^2g^2) + (a^2 + ag^2 + aq^2 + ap^2 + ah^2) \\
& + (b^2 + b^3 + bg^2 + bq^2 + bp^2 + bh^2) + (c^2 + c^2g^2 + c^2q^2) + (d^2 + e^2 + dg^2 + dp^2 + dh^2 + dph + ep^2 + eh^2). \quad (12)
\end{aligned}$$

First bracket in Eq. (12) corresponds to the X_3 and Δ_5 IRs and their couplings (see Table I). We anticipate that the lowest coupling term between them g^2q^2 must be large and should lower the free energy \mathcal{F} . Second bracket corresponds to Δ_2 and Δ_4 IRs and to the coupling terms among them. The second line in Eq. (12) describes the coupling of IR X_1 with the primary OPs, being of linear-quadratic form. The interaction between the X_1 and Δ_5 phonons discussed by Iizumi⁶⁹ is described by the fq^2 term. The following terms given in fourth, fifth, sixth and seventh brackets determine the coupling of IRs of the crystal point groups A_{1g} , E_g , T_{1g} , and T_{2g} , respectively, with the primary OPs. Again their forms are adequate to describe the influence of secondary OPs on the transition. In particular, the term dg^2 in the last line, describing the coupling between the X_3 and T_{2g} OPs, contributes to the softening of the c_{44} elastic constant.³⁶ Other couplings involving the zone-center IRs may account for anomalies observed by the Raman studies.^{48,49}

In order to identify the relevant part of the free energy Eq. (12) which drives the VT in magnetite, we consider next the changes of the electronic structure (Sec. III) and the phonon spectra (Sec. IV) at the transition. In fact, we shall demonstrate below that these properties are strongly coupled to each other, and the VT is driven by the electron-phonon interaction enhanced by the local Coulomb interaction U , see Sec. V.

III. ELECTRONIC STRUCTURE

A. Computational methods

The lattice parameters of Fe_3O_4 were optimized together with the electronic structure using the total energy DFT approach. The numerical calculations were performed by means of the VASP program⁷⁰ within the GGA+ U approach.⁷¹ The program uses highly accurate full-potential projector-augmented wave (PAW) method, originally proposed by Blöchl⁷² and implemented by Kresse and Joubert.⁷³ The wavefunctions in the core region are obtained by the linear transformation from variational pseudo-wavefunctions. In the augmented region the wavefunctions are expanded in the plane wave basis. Two supercells with the periodic boundary conditions were chosen: $a \times a \times a$ and $a/\sqrt{2} \times a/\sqrt{2} \times 2a$ for the $Fd\bar{3}m$ and $P2/c$ structures, respectively, with 56 atoms each. The latter supercell was used also for the reference system of $Fd\bar{3}m$ symmetry, when total energies of two considered structures were compared.

For a given ionic configuration, the Kohn-Sham Hamiltonian was diagonalized by the iterative residual minimization method,⁷⁰ which allows one for efficient optimization of the charge density and wavefunctions. In the initial steps also the blocked Davidson minimization method was applied. To improve convergence a small smearing of electronic states at the Fermi surface was introduced with the effective parameter $\sigma = 0.2$ eV. The Monkhorst-Pack scheme⁷⁴ was applied for summation over two \mathbf{k} -point grids $6 \times 6 \times 6$ and $6 \times 6 \times 2$ relevant for $Fd\bar{3}m$ and $P2/c$ symmetries, respectively, which are large enough for a meaningful energy comparison. In Ref. 60 we used the smaller grids, i.e., $4 \times 4 \times 4$ and $4 \times 4 \times 2$, which give already satisfactory values for lattice parameters and energies. However, larger \mathbf{k} -point grids were used at present to reach a higher accuracy as they give even more reliable values of force constants and phonon frequencies. The energy cut-off for the plane wave expansion was set at 520 eV after we have verified that the contribution of states with higher energies was negligible.

The local electron interactions between $3d$ electrons on Fe ions were included in the Hartree-Fock approximation, as usually done in the LDA+ U method.²⁵ As a result one finds the total energy of the system E_{tot} in the form

$$E_{\text{tot}} = E_{\text{GGA}} + E_U - E_{\text{dc}}, \quad (13)$$

where E_{GGA} is the energy obtained in the GGA approach, E_U describes the contribution due to local interactions parametrized by the Coulomb element U and Hund's exchange J , and E_{dc} is the double counting correction term, i.e., the averaged electron-electron interaction, which has to be subtracted. The details of the Hamiltonian used in the calculations were presented in Ref. 75.

In the present calculations we have chosen the following parameters: $U = 4.0$ eV and $J = 0.8$ eV. The value of U agrees with the constrained DFT calculations,^{23,58} and is somewhat reduced from the ionic value of 6.4 eV estimated by Zaanen and Sawatzky.⁷⁶ The value of J was obtained from the atomic values of the Racah parameters for Fe^{2+} ions:⁷⁶ $B = 0.131$ eV and $C = 0.484$ eV. Here we use an average value of Hund's exchange,⁷⁷ $J = \frac{5}{2}B + C$, as usually implemented within the LDA+ U method.⁷⁸ Note that the value of $J = 1.0$ eV used in some LSDA+ U calculations⁷⁹ and in the LDA+DMFT method⁵⁸ is somewhat overestimated (in fact this value applies to a pair of e_g electrons rather than to a pair of t_{2g} electrons). The nearest-neighbor Coulomb interaction is one order of magnitude smaller $V \simeq 0.3 - 0.4$ eV,²³ and we assume that it is to a large extent included already in

the GGA scheme.

The optimal atomic configuration, which gives the minimum of the total energy, $E_0 = \min\{E_{\text{tot}}\}$, was found using the conjugate gradient and quasi-Newton procedures.⁷⁰ Because of phonon calculations, which are based on the well-optimized supercell, the terminating criteria for the electronic and ionic degrees of freedom were very strict: 10^{-7} eV and 10^{-5} eV, respectively. To get more precise atomic positions we used also force criterion, in quasi-Newton procedure, which allowed us to get residual forces less than 10^{-2} meV/Å (the pressure was then less than 0.1 kbar).

Phonon frequencies were calculated only for the cubic structure, using the direct method⁶¹ implemented in the PHONON program.⁸⁰ According to the Hellmann-Feynmann (HF) theorem, the atomic forces can be obtained by displacing atoms from their equilibrium positions. The minimum number of displacements depends on crystal symmetry and on the number of nonequivalent atoms. For magnetite only three independent displacements for Fe(A), Fe(B), and O atoms are sufficient. To minimize systematic errors we performed displacements in positive and negative directions.

The combination of derived displacements and forces allows one to obtain the force constants matrix elements by the singular value decomposition method. A special treatment was applied for calculations with finite U , where the convergence of the electronic part was in some cases very slow. When this occurred, the calculations of the HF forces were initialized using the wavefunctions optimized for the cubic structure. For magnetite, the direct method provides exact frequencies at the Γ and X points. The phonon frequencies at other points were evaluated with only small errors due to large supercell used in the present calculations.

B. Crystal optimization

The structural properties of the cubic and monoclinic phases have been discussed in many previous studies. In Tabs. IV and V we summarize the electronic and lattice parameters obtained in the present calculations, comparing them with the experimental data. We focused mainly on the effects connected with the Coulomb interaction U . For the cubic symmetry, the lattice constant a and the internal oxygen parameter x depend rather weakly on U , and show overall good agreement with experimental data of Refs. 15,56,81,82 (Table IV). As expected and noticed before,⁸³ the magnetic moments on particular atoms increase with U , improving the agreement between the electronic structure calculations and the experimental data. The average magnetic moment per one formula unit m_{av} , however, does not change with U and J . It shows that magnetic polarization in this material is already at maximum and can be therefore well described in the band picture, while reliable calculations concerning the magnetic polarization of individual Fe ions require local electron

TABLE IV: Ground state lattice and electronic parameters for $Fd\bar{3}m$ and $P2/c$ structures. The magnetic moments of individual ions Fe(A) (m_A), Fe(B) (m_B), and O (m_O) obtained within the present GGA ($U = J = 0$) and GGA+ U (with $U = 4.0$ eV and $J = 0.8$ eV) calculations for the high-temperature $Fd\bar{3}m$ phase are compared with the experimental data, wherever available. The lattice constants (a, b, c) are in Å, magnetic moments μ_i in μ_B , and energies E_{tot} and the gap Δ_g in eV.

phase	quantity	GGA	GGA+ U	experiment
$Fd\bar{3}m$	a	8.377	8.446	8.394 ^a
	x	0.2545	0.2549	0.2549 ^a
	m_A	-3.40	-3.97	-3.82 ^b
	m_B	3.52	3.87	
	m_O	0.08	0.04	
	m_{av}	3.96	3.96	4.05 ^c
	E_{tot}	-426.39	-386.80	
	Δ_g	0	0	
$P2/c$	a	5.926	5.967	5.944 ^a
	b	5.926	5.995	5.925 ^a
	c	16.752	17.034	16.775 ^a
	β	90.004	90.417	90.237 ^a
	E_{tot}	-426.63	-389.28	
	Δ_g	0	0.33	0.14 ^d

^a Reference 15

^b Reference 81

^c Reference 82

^d Reference 56

interactions $\{U, J\}$. One finds that magnetite is metallic ($\Delta_g = 0$) in the cubic phase, independently of the actual values of U and J . Note that the total ground state energy of the crystal E_{tot} increases with U , but direct comparison between the energies obtained in the GGA and the GGA+ U is meaningless.

The $P2/c$ structure was optimized starting from the experimentally determined geometry,¹⁵ but we did not impose orthorhombic $Pmca$ symmetry constraints on atomic positions. The theoretical crystal structures, obtained also by the VASP program, were already discussed in detail in Ref. 84. We note that some discrepancies between the results of these two calculations may follow from different energy cut-off and termination conditions, as well as from slightly different values of U and J used. In the GGA calculations performed with $U = J = 0$, the lattice constants, atomic positions, and the total energy converge to those of the high-symmetry cubic structure (Tabs. IV and V). This behavior agrees with the molecular dynamics simulations presented in Ref. 59. The proximity of the total energies E_{tot} obtained in both phases indicates that by going beyond the GGA one of these structures will be stabilized. Note that the energy difference between these two phases obtained in the GGA calculations is too small to arrive at definite conclusion concerning the stability of the LT phase of $P2/c$ symmetry.

Indeed, the optimization performed with $U = 4.0$ eV and $J = 0.8$ eV gives lower total energy of the $P2/c$

TABLE V: Atomic positions for iron ions (at A and B sites) and oxygen ions in the $P2/c$ structure, as obtained in the GGA calculations (left, $U = J = 0$) and in the GGA+ U calculations (middle, with $U = 4.0$ eV and $J = 0.8$ eV), compared with the experimental data of Ref. 15 (right).

atom	$U = J = 0$			$U = 4.0$ eV, $J = 0.8$ eV			Experiment ¹⁵		
	x	y	z	x	y	z	x	y	z
A1	0.2490	0.0	0.0625	0.2491	0.0104	0.0637	0.25	0.0034	0.0637
A2	0.25	0.5	0.1875	0.2493	0.4991	0.1885	0.25	0.5061	0.1887
B1a	0.0	0.5	0.0	0.0	0.5	0.0	0.0	0.5	0.0
B1b	0.5	0.5	0.0	0.5	0.5	0.0	0.5	0.5	0.0
B2a	0.0	0.0	0.25	0.0	0.0050	0.25	0.0	0.0096	0.25
B2b	0.5	0.0	0.25	0.5	0.9996	0.25	0.5	0.0096	0.25
B3	0.25	0.25	0.375	0.2502	0.2604	0.3804	0.25	0.2659	0.3801
B4	0.25	0.75	0.375	0.2529	0.7553	0.3740	0.25	0.7520	0.3766
O1	0.25	0.2591	-0.0023	0.2508	0.2689	0.0000	0.25	0.2637	-0.0023
O2	0.25	0.7408	-0.0023	0.2491	0.7572	-0.0026	0.25	0.7461	-0.0029
O3	0.25	0.2409	0.2523	0.2487	0.2370	0.2541	0.25	0.2447	0.2542
O4	0.25	0.7591	0.2523	0.2482	0.7708	0.2474	0.25	0.7738	0.2525
O5a	-0.0091	0.0	0.1272	-0.0155	0.0045	0.1297	-0.0091	0.0095	0.1277
O5b	0.4909	0.0	0.3727	0.4941	0.0187	0.3701	0.4909	0.0095	0.3723
O6a	-0.0092	0.5	0.1227	-0.0083	0.4911	0.1257	-0.0081	0.5046	0.1246
O6b	0.4908	0.5	0.3772	0.4842	0.5042	0.3730	0.4919	0.5046	0.3754

structure by about 2.48 eV compared to the cubic phase. This result confirms that the monoclinic structure is more stable in the low temperature regime. The obtained insulating gap $\Delta_g = 0.33$ eV is larger than the experimental value 0.14 eV, but is close to the values obtained in other electronic structure calculations.⁵⁹ One should note that the calculated gap is usually larger for the relaxed system than for the experimental geometry.

The charge and spin distribution in the $3d$ states on Fe(B) ions is presented in Table VI. Since we have chosen larger Wigner-Seitz radius $r_{WS} = 1.5$ Å, the obtained values are somewhat larger than in other studies.^{29,30} However, the difference between the larger ($B1$ and $B4$) and smaller ($B2$ and $B3$) charges ($\sim 0.2e$) is similar, and agrees well with experiment.¹⁵ The electron density of states (DOS) and the orbital density distribution will be analyzed in Sec. V, where the EP interactions are discussed.

The parameters of the relaxed crystal structure show good agreement with experiment.¹⁵ The lattice constants are overestimated only by about 1%, and the monoclinic angle is well reproduced. As in the real crystal of magnetite, the atoms are displaced predominantly along the y direction with respect to the original cubic positions. In the monoclinic cell, the y direction corresponds to the $[110]$ diagonal one in the $Fd\bar{3}m$ symmetry. According to the experiment,¹⁵ the largest atomic shift of 0.13 Å is found for Fe($B3$) ions, and it agrees well with the theoretical value 0.11 Å. Displacements of Fe($B2$) and Fe($B4$) ions are much smaller (0.03-0.04 Å), and Fe($B1$) ions do not change their positions at all. As observed experimentally, the Fe(A) ions have only minor displacements (~ 0.03 Å), and they are smaller than those found theoretically (0.05 Å). The largest shift of oxygen ions amounts to 0.11 Å, and is slightly larger than the exper-

imental value found for O4 ions, being 0.09 Å.

This present analysis shows that the largest atomic displacements, leading to the monoclinic phase, are connected with Fe(B) and O ions. They induce deformations of Fe $_B$ O $_6$ octahedra. It shows that models which assume only oxygen vibrations are probably not sufficient to describe fully all relevant degrees of freedom involved in the Verwey phase transition. In Secs. IV and V we will study the phonon spectrum, and in particular we will focus on those modes, which strongly influence the electronic and crystal structure.

C. Effect of Hund's exchange

We close this Section by investigating the effect of Hund's exchange on the electronic structure for fixed $U = 4.0$ eV. One finds that the gap value is considerably enhanced for $J = 0$ ($\Delta_g = 0.54$ eV) over the value found for the realistic exchange interaction $J = 0.8$ eV

TABLE VI: Gap in the electronic structure Δ_g (in eV), and the charge and magnetization densities for nonequivalent Fe(B) atoms, n_{Bi} and m_{Bi} , as obtained in the $P2/c$ phase with $U = 4.0$ eV for two values of Hund's exchange: $J = 0.8$ eV (left) and $J = 0$ (right).

J	0.8		0.0	
	Δ_g		Δ_g	
atom B	n_{Bi}	m_{Bi}	n_{Bi}	m_{Bi}
$B1$	6.07	3.64	6.09	3.66
$B2$	5.85	4.05	5.82	4.15
$B3$	5.87	4.00	5.85	4.09
$B4$	6.09	3.62	6.11	3.64

($\Delta_g = 0.54$ eV), see Table VI. This demonstrates that the gap opens between the minority subbands and the actual effective interaction between the electrons with the same spins is reduced by the exchange term. When Hund's exchange is missing, this interaction is enhanced, resulting in an increased gap value. Note that the effective interaction ($U - J$) between the electrons of the same spin decides also about the magnetic and phonon properties of the iron metal.⁷⁵

The charge density distribution $\{n_{Bi}\}$ over the iron ions in B positions is only little modified when $J = 0$ is selected. In fact, the polarization between the amplitude of the CO between the $\{B1, B4\}$ and $\{B2, B3\}$ pairs of ions is somewhat increased which again confirms that the effective interaction between the minority electrons has increased. Consequently, the magnetic moments m_{Bi} are also slightly increased for $J = 0$ over their values found for $J = 0.8$ eV. This behavior allows us to conclude that the calculations^{58,79} performed with the same value of $U = 4.0$ eV but with larger $J = 1.0$ eV correspond in fact to *weaker* interaction between the minority electrons.

IV. LATTICE DYNAMICS

In this Section, we analyze the lattice dynamics of magnetite in the cubic phase. The low-energy dispersion curves were presented already in the previous paper.⁶⁰ Here we extend this study by a detailed discussion of

the phonon modes at the zone center and analyze the effects related to electron correlations. In the Γ point there are 42 modes classified according to the IRs of the cubic symmetry group,

$$\Gamma = A_{1g} + 2A_{2u} + E_g + 2E_u + T_{1g} + 3T_{2g} + 5T_{1u} + 2T_{2u}. \quad (14)$$

There are four optic infrared modes with T_{1u} symmetry, five Raman modes with A_{1g} , T_{2g} , and E_g symmetries, respectively, and seven silent modes. In Table VII we compare the frequencies of the optic modes with the experimental data from the neutron, infrared, and Raman measurements. Two sets of theoretical frequencies obtained from the calculations with: (i) $U = 0$ and $J = 0$ called below $U = 0$, and (ii) $U = 4.0$ eV and $J = 0.8$ eV called below $U = 4$ eV, are presented. The lowest optic mode at 18.5 meV with T_{2u} symmetry (previously assigned as T_{2g}) was measured by the neutron scattering.³⁸ Four infrared modes with T_{1u} symmetry have been measured by Degiorgi *et al.*⁴⁷ Two lowest ones (at 12 and 32 meV) have very low intensities and large widths in experiment, so they can be hardly compared with the theoretical values. For the other two modes (at 42.5 and 67.2 meV) the agreement between the experiment and the present calculations is very good. In fact, in a broad range the frequencies ω_n of these modes are almost independent of U , but finite U is of importance to improve the agreement with experiment for the mode observed at $\omega = 42.5$ meV.

The theory shows that two frequencies around 40 meV are very close to each other, and it may be the reason of apparent difficulties in resolving these infrared modes. This interpretation could be supported by the fact that the peak observed in spectroscopy at 42.5 meV seems to be indeed very broad.⁴⁷ As a success of the present theory one finds that all computed Raman modes show good agreement with experimental data. In two cases (for A_{1g} and E_g modes), calculations with finite $U = 4.0$ eV largely improve this agreement. The only discrepancy found is the reversed assignment of symmetries (E_g and T_{2g}) of the two modes at ~ 39 and ~ 50 meV.^{48,49} At present we cannot explain this discrepancy and we hope that future experiments would verify the present prediction of the theory.

Computed phonon frequencies show rather strong dependence on U . Interestingly, the frequencies *increase*, in spite of larger lattice constant for $U > 0$ which suggests the opposite trend. This indicates a strong effect of local Coulomb interactions on lattice dynamics via respective changes in the electronic density distribution and in the value of EP coupling. It can be understood using a simple picture explained below. In the presence of local correlations, the electron localization in Fe($3d$) orbital states is enhanced. It results in weaker screening of ionic interactions and, consequently, in larger interatomic forces. Since phonon frequencies depend directly on force constants, their values increase. This mechanism is supported by the observation that the phonon modes stiffen in the insulating state in spite of lattice expansion due

TABLE VII: Phonon frequencies ω_n at the zone center compared with the experimental data of Refs. 38, 47, 48, and 49 (all in meV). I and R denotes infrared and Raman active modes, respectively. The difference in phonon frequency due to local interactions $\delta\omega$ is given in percents.

Γ	active	ω_n		$\delta\omega$	Experiment
		$U = 0$	$U = 4.0$ eV		
T_{2u}		16.84	17.68	5.0	18.5 ^a
T_{1u}	I	19.98	21.46	7.4	12 ^b
E_u		21.10	22.71	7.0	
T_{2g}	R	24.16	25.77	6.7	23.93 ^c , 23.93 ^d
E_g	R	32.87	41.76	27.0	39.43 ^b , 38.19 ^c , 37.20 ^d
T_{1g}		33.10	39.27	18.6	
A_{2u}		35.53	38.08	7.2	
T_{1u}	I	38.31	40.10	4.7	32 ^b
T_{1u}	I	40.03	42.85	7.0	42.5 ^b , 43.4 ^c
T_{2u}		42.72	45.31	6.1	
T_{2g}	R	49.61	55.22	11.3	50.83 ^b , 50.83 ^d
E_u		52.50	54.30	3.4	
T_{2g}	R	65.10	68.89	5.8	67.20 ^b , 66.95 ^c , 66.95 ^d
T_{1u}	I	66.77	66.24	0.8	68 ^b , 69.43 ^c
A_{1g}	R	73.06	82.74	13.2	83.32 ^b , 83.07 ^c , 82.95 ^d
A_{2u}		74.21	81.33	9.6	

^a Reference 38

^b Reference 47

^c Reference 48

^d Reference 49

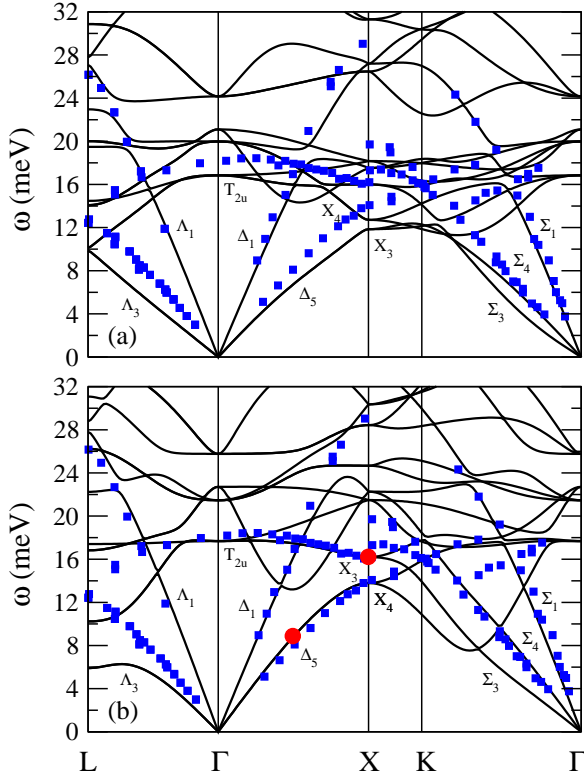


FIG. 2: (Color online) Low-energy phonon frequencies ω as obtained for the cubic phase of Fe_3O_4 with: (a) $U = J = 0$, and (b) $U = 4.0$ eV and $J = 0.8$ eV. The squares show the experimental data obtained by neutron scattering.³⁸ Two primary OPs are related to Δ_5 and X_3 phonons marked by circles in (b). The high symmetry points from left to right in units of $\frac{2\pi}{a}$ are: $L = (\frac{1}{2}, \frac{1}{2}, \frac{1}{2})$, $\Gamma = (0, 0, 0)$, $X = (0, 0, 1)$, $K = (\frac{1}{2}, \frac{1}{2}, 1)$, $\Gamma = (1, 1, 1)$.

to the monoclinic distortion.^{48,49,51} One should note also that two Raman modes at frequencies ~ 39 meV (E_g) and ~ 83 meV (A_{1g}), which strongly depend on U , show the largest anomalies at the transition point.^{48,49} In contrast, for the infrared phonons the frequency dependence on U is much weaker and no significant anomalies were found at T_V , apart from some changes in the linewidths of these modes.⁴⁸

The phonon dispersion relations were calculated along the main directions of the reciprocal space. In Tab. VIII we present the compatibility relations for the IRs in the Γ point and along three directions: $\Delta[001]$, $\Sigma[110]$, and $\Lambda[111]$. They show how the degenerate IRs split when symmetry is reduced. Knowing these relations, the symmetries of all dispersion curves can be properly assigned. Fig. 2 presents the lowest dispersion curves obtained for $U = 0$ and $U = 4.0$ eV, compared with the neutron scattering data.³⁸ Longitudinal acoustic modes agree very well with experimental values, almost independently of the actual value of U (the data for intermediate values of U are not shown). This behavior demonstrates that these modes couple very weakly to electronic

TABLE VIII: Compatibility relations between the Γ point and Δ , Σ and Λ directions, as well as the X point and Δ , Σ directions.

Γ, X	$\Delta [001]$	$\Sigma [110]$	$\Lambda [111]$
A_{1g}	Δ_1	Σ_1	Λ_1
A_{2u}	Δ_4	Σ_3	Λ_1
E_g	$\Delta_1 \oplus \Delta_2$	$\Sigma_1 \oplus \Sigma_3$	Λ_3
E_u	$\Delta_3 \oplus \Delta_4$	$\Sigma_2 \oplus \Sigma_3$	Λ_3
T_{1g}	$\Delta_1 \oplus \Delta_5$	$\Sigma_1 \oplus \Sigma_3 \oplus \Sigma_4$	$\Lambda_1 \oplus \Lambda_3$
T_{2g}	$\Delta_4 \oplus \Delta_5$	$\Sigma_1 \oplus \Sigma_2 \oplus \Sigma_3$	$\Lambda_1 \oplus \Lambda_3$
T_{1u}	$\Delta_1 \oplus \Delta_5$	$\Sigma_1 \oplus \Sigma_3 \oplus \Sigma_4$	$\Lambda_1 \oplus \Lambda_3$
T_{2u}	$\Delta_2 \oplus \Delta_5$	$\Sigma_1 \oplus \Sigma_2 \oplus \Sigma_4$	$\Lambda_2 \oplus \Lambda_3$
X_1	$\Delta_1 \oplus \Delta_4$	$\Sigma_1 \oplus \Sigma_3$	
X_2	$\Delta_2 \oplus \Delta_3$	$\Sigma_2 \oplus \Sigma_4$	
X_3	Δ_5	$\Sigma_3 \oplus \Sigma_4$	
X_4	Δ_5	$\Sigma_1 \oplus \Sigma_2$	

density distribution, and are therefore not sensitive to changes in electronic structure. A radically different behavior is observed for the transverse acoustic and optic phonons, which strongly depend on U . The most significant changes were obtained here in the Δ and Λ directions. So far, we could not find a good physical explanation for a large discrepancy between theory and experiment observed at the L point.

For the lowest acoustic and optic Δ_5 modes, the agreement improves in case of $U = 4$ eV. It is quite remarkable that the optic mode behaves differently in both cases. For $U = 0$ this mode crosses with another Δ_5 mode, so the sequence of phonon branches is interchanged. This behavior is responsible for the apparent discrepancies between the frequencies of phonon modes in theory and experiment for the $U = 0$ case. According to the experiment,³⁸ the lowest phonon at the X point has the X_4 symmetry, and splits into the Σ_1 and Σ_2 phonon branches along the $[110]$ direction (see Table VIII). The second lowest mode has X_3 symmetry and transforms into the Σ_3 and Σ_4 modes. This order is indeed accurately reproduced by the GGA+ U calculations with realistic local Coulomb interactions (i.e., taking $U = 4.0$ eV and $J = 0.8$ eV). In contrast, in the $U = 0$ case, the order of the lowest modes is reversed. It shows that Coulomb interactions strongly modify lattice dynamics and the phonon energy spectrum. We thus emphasize that they have to be included to obtain not only quantitative but even qualitative agreement with experiment.

V. ELECTRON-PHONON INTERACTION

A. Instability of the cubic phase

Having obtained phonon dispersion curves and their symmetries, we now focus on the effects induced by phonons, especially on the OPs derived in Sec. II. In this Section, we discuss the EP interactions associated with the X and Δ phonons, and present the instabil-

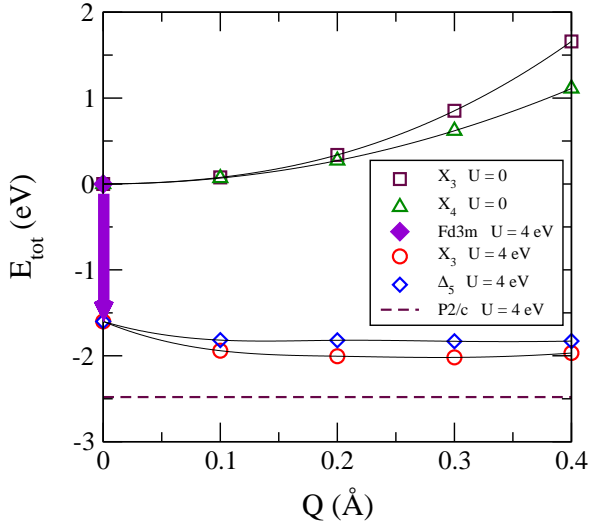


FIG. 3: (Color online) Total energy E_{tot} (13) as a function of the amplitude Q of phonon modes with the X_3 , X_4 , and Δ_5 symmetries (in Å), as obtained with ($U = 4$ eV) and without ($U = 0$) local Coulomb interactions at Fe ions. The energy gain of ~ 1.6 eV due to the orbital polarization at $Q = 0$ is indicated by the arrow.

ity of the cubic phase triggered by local deformations. Since one expects the strongest effects for the low energy phonons, we analyze only the lowest energy acoustic and optic branches.

First, for \mathbf{k}_X wave vector we compare the EP coupling for the lowest X_3 and X_4 modes. At the \mathbf{k}_X point all modes are doubly degenerate, so we used polarization vectors from only one branch by shifting the wavevector to $\mathbf{k}_X + \delta\mathbf{k}_\Sigma$, removing then the degeneracy. In Fig. 3 we present the total energy E_{tot} of the distorted cubic structure as a function of the increasing phonon amplitude Q . The energies of relaxed (undistorted) crystals obtained in the GGA and GGA+ U calculations were shifted to a common energy origin for a more transparent presentation (their actual values can be found in Table IV). One finds that for $U = 0$ the energy increases when the cubic structure is distorted by either X_3 or X_4 phonon. This behavior is characteristic and represents a typical situation when atoms are displaced from their respective equilibrium positions. It simply confirms that the cubic symmetry is the most stable structure for $U = 0$, and does not undergo any instability towards other possible symmetries.

In the GGA+ U calculations, the situation changes drastically since the orbital degrees of freedom becomes active and influence the electronic structure. As demonstrated in Ref. 59, the orbital polarization breaks the symmetry of wavefunctions within the cubic $Fd\bar{3}m$ structure and leads to lowering of the total energy. This effect was demonstrated by initializing the self-consistent procedure using the wavefunctions of the $C2/C$ structure.⁵⁹ Applying a similar procedure, we have started calculations with the wavefunctions of the low-symmetry

$P2/c$ phase and optimized the electronic structure self-consistently in the $Fd\bar{3}m$ structure. The reference energy obtained by the direct optimization is denoted by the point at $E_{\text{tot}} = 0$ in Fig. 3, and the decrease due to orbital polarization (about 1.6 eV) is visualised by the arrow. The lowering of the ground state energy is associated with a partial CO and OO which arises in the t_{2g} states, however, it does not generate the gap opening yet. In fact, the calculation suggests that this is rather a metastable state, showing only short-range charge-orbital correlations without well defined symmetry.

Total energy E_{tot} decreases further from that obtained for the state with CO and OO induced by finite Coulomb interactions for increasing phonon distortion Q (see Fig. 3), which leads eventually to the metal-insulator transition. The strongest decrease of the total energy was found for the X_3 mode. On the contrary, by considering a single X_4 phonon amplitude we have verified that this type of distortion does not induce any energy decrease. Instead, the acoustic Δ_5 phonon mode leads to the energy lowering when local Coulomb interactions are present. Therefore, we included in Fig. 3 also the energy dependence for this acoustic mode. The energy decrease is here smaller than in case of the X_3 mode. Note however that because of double degeneracy the total energy may also depend on the phase. Finally, the groundstate energy for the $P2/c$ symmetry is shown in Fig. 3 as the lowest dashed line. Since the lattice deformation induced by either X_3 or Δ_5 mode is not sufficient to lower the energy to this level, other OPs have to be active as well.

B. Metal-insulator transition

The changes in the electron DOS induced by the considered phonon modes at the \mathbf{k}_X point are presented in Fig. 4. They are compared with the respective DOS found for the undistorted structures with $Fd\bar{3}m$ and $P2/c$ symmetry, respectively. The results of the calculations performed in the GGA and in the GGA+ U approach are shown on the left and right hand side of Fig. 4, respectively. The main effect of finite U for the cubic structure is to increase the exchange splitting between the up and down spin states, cf. Figs. 4(a) and 4(e). The up-spin states at Fe(B) ions and down-spin states at Fe(A) ones are shifted to lower energies below E_F . In addition, finite U decreases the spectral density of minority t_{2g} states just above E_F . This indicates the enhancement of electron localization due to local electron interactions, which leads to gap opening in the distorted structure.

First observation connected with the EP interaction is that the overall effects of X_3 and X_4 distortion are much weaker for the uncorrelated ($U = 0$) case than for the correlated ($U = 4.0$ eV) one. Comparing these two distortions for $U = 0$ [Figs. 4(b) and 4(c)], we see that the strongest coupling is associated with the X_3 phonon. Especially for down-spin states above E_F one finds a de-

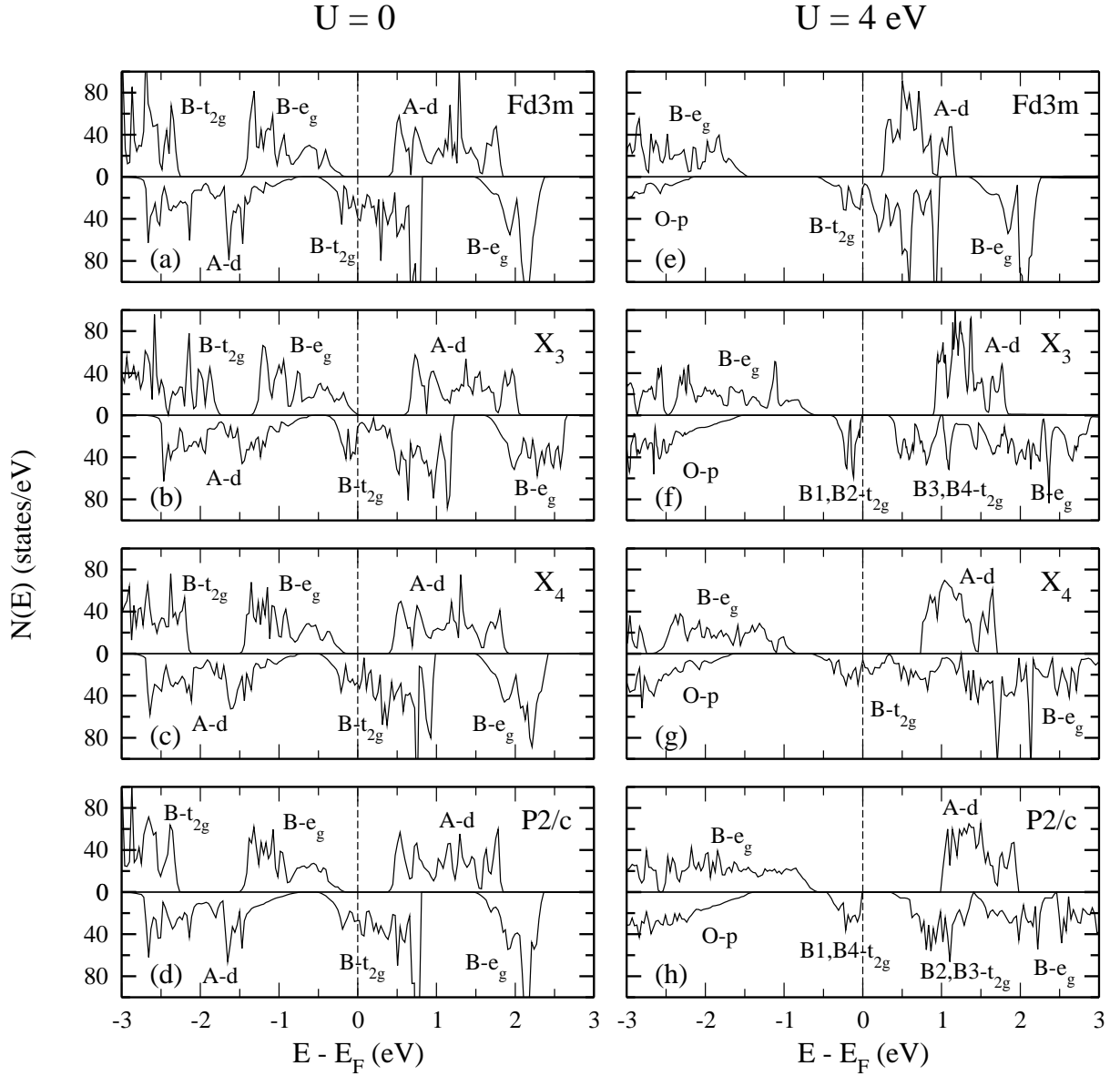


FIG. 4: Electronic DOS for the spin-up (top) and spin-down (bottom) electrons in the phases of $Fd\bar{3}m$, $Fd\bar{3}m+X_3$, $Fd\bar{3}m+X_4$, and $P2/c$ symmetry, as obtained in: (a)–(d) GGA ($U = 0$), and (e)–(h) GGA+ U (with $U = 4.0$ eV) calculations.

crease of the spectral density. This instability is connected with the \mathbf{k}_X nesting vector at the Fermi surface, as discussed some time ago by Yanase and Hamada.²⁴ It is quite remarkable that this effect alone does not suffice to induce a metal-insulator transition, but such a transition is triggered when it is amplified by local Hubbard interaction U . Indeed, when the X_3 distortion is made in presence of finite U [Fig. 4(f)], the gap opens at E_F , and the metal-insulator transition takes place. Note that apart from some subtle differences, the distribution of the spectral weight near E_F found with the X_3 distortion is quite similar to that found in the $P2/c$ phase [Fig. 4(h)].

Surprisingly, the X_4 mode does not produce a similar effect, although the changes of the electron DOS were here similar to those due to X_3 for $U = 0$, and the EP

coupling is here also much stronger than for $U = 0$. This result agrees perfectly with the group theory analysis of Sec. II, showing that X_3 is the primary OP and X_4 is neither primary nor secondary OP for the VT. We remark that the influence of the Δ_5 mode on the DOS has been discussed previously,⁶⁰ and it does not induce the insulating gap either in spite of its significant coupling to the electronic density. Thus, we conclude that the X_3 mode plays the decisive role in the metal-insulator transition which accompanies the VT.

C. Charge and orbital order

Realistic treatment of the charge and orbital order requires the electronic structure calculations with finite local Coulomb interactions using LSDA+ U -like methods. The electronic DOS in the cubic phase [Fig. 4(e)], as well as earlier experimental studies,⁸⁵ suggest that magnetite is an itinerant magnet and not a mixed valent system. The VT is therefore not due to freezing of charge fluctuations at Fe(B) ions, but rather due to the symmetry change, which leads only to weak CO as a consequence of the undergoing phase transition. This scenario is confirmed by the changes in the electron DOS above and below the VT, as the gap at the Fermi energy induced by the X_3 phonon [see Fig. 4(f)] splits the t_{2g} band into the occupied states at the $B1$ and $B2$ Fe ions and empty states at the $B3$ and $B4$ ions. Thus, this mode is responsible for the charge disproportionation which persists also in the $P2/c$ phase [Fig. 4(h)]: increased t_{2g} electron density for $\{B1, B2\}$ ions and reduced density for $\{B3, B4\}$ ions. Note that four Fe(B) sites split into two subclasses as a result of the lattice distortion in the X_3 mode [Fig. 5(a)]. The amplitude of the charge (spin) disproportionation is comparable with that found for the $P2/c$ symmetry (see Table VI). Interestingly, this CO pattern is *similar* to that proposed originally by Verwey and fulfills the Anderson criterion. These findings agree also with other LSDA+ U and GGA+ U calculations.^{29,59,79}

In addition, we have found that the X_3 mode stabilizes the OO in the t_{2g} states. The resulting orbital polarization with atomic displacements is presented in Fig. 5(a). In the considered mode the atoms vibrate along the $[110]$ direction, and the dominating components are those connected with distortions of Fe(B) ions and oxygen ions in the same planes. Oxygen displacements are 65% of Fe(B) displacements, while Fe(A) atoms shift only by about 23% of them (not shown). The considered mode is limited to single Fe–O planes: Fe(B) ions move along with O ions in one plane, while atoms in neighboring planes do not move at all (they participate in the other X_3 branch in the perpendicular direction). This deformation modifies distances between Fe(B) atoms and oxygens situated above and below them, inducing changes in the electron density distribution within t_{2g} states and a coexisting charge and orbital order in the $B1$ and $B2$ chains. As indicated in Fig. 5, electrons occupy orthogonal d_{yz} and d_{xz} orbitals, thus forming the state with alternating OO.

This coexisting charge-orbital order and the insulating gap induced by the X_3 mode has to be compared with that observed in the monoclinic phase of $P2/c$ symmetry [Fig. 5(b)]. The electronic DOS for this symmetry is presented in Fig. 4(h). The magnitude of the gap is similar to the gap generated by the X_3 phonon mode shown in Fig. 4(f), however, the occupied states below E_F belong now to the $\{B1, B4\}$ ions and empty states to the $\{B2, B3\}$ ones. Actually, Fe(B) ions are split into two groups $\{B1, B4\}$ and $\{B2, B3\}$, as average Fe–O distances for the bonds to the $\{B2, B3\}$ sites are

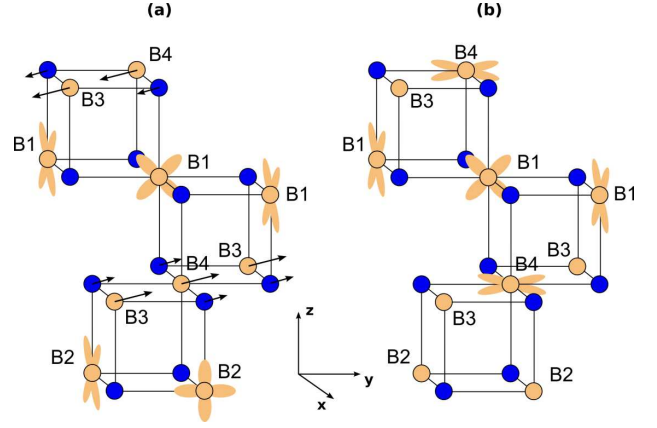


FIG. 5: (Color online) Orbital order in the t_{2g} states of Fe(B) ions in magnetite as found for: (a) the $Fd3m$ cubic structure distorted by the X_3 phonon, and (b) the structure of $P2/c$ symmetry. The balls indicate Fe and O ions in the respective crystal structure, with the same meaning of colors as in Fig. 1. The arrows in (a) represent the atomic displacements in the X_3 mode.

significantly smaller than those for the $\{B1, B4\}$ ones. Therefore, the CO has to change from that promoted by the X_3 mode alone. Surprisingly, the weak CO found in the LT monoclinic phase does not satisfy the Anderson criterion, but plays no role in the actual mechanism of the transition.

The corresponding orbital pattern also has changed [see Fig. 5(b)]. The occupied states on $B1$ and $B4$ ions form the alternating OO with the orthogonal orbitals on the nearest neighbor iron sites. We emphasize that in the $P2/c$ frame, the occupied t_{2g} states are given by $\frac{1}{\sqrt{2}}(d_{xz} \pm d_{yz})$ and $d_{x^2-y^2}$ combinations. Therefore, on comparing Figs. 5(a) and 5(b), we conclude that the X_3 mode demonstrates a generic tendency towards the OO within the t_{2g} minority states, but only partly explains the observed OO in the LT phase with $P2/c$ symmetry. This is however quite natural and expected, since the X_3 mode is only one component of the OPs that condense at the VT, which *all* finally lead to the change of symmetry to the LT monoclinic phase.

In the next step, one should consider the superposition of the X_3 with the Δ_5 mode. The latter one is crucial to explain the doubling of the unit cell and the observed charge-orbital pattern. As we mentioned before, this mode is double degenerate and the atomic displacements depend on the phase. So, a detailed analysis of the EP coupling, similar to that presented above for the X_3 modes, is rather difficult. Moreover, because of the system complexity, it is likely that the atomic displacements belonging to the secondary OPs are also involved in the final charge-orbital order. In spite of these difficulties, the studies presented in this Section demonstrate how the phonons interplay with charge and orbital degrees of freedom in the VT.

VI. MECHANISM OF THE VERWEY TRANSITION

From the results presented in the previous Section and from the earlier experimental studies, it is clear that the mechanism of the VT includes two essential ingredients: (i) strong intraatomic Coulomb interactions $\{U, J\}$ at Fe ions, and (ii) phonon-driven lattice instability. On the one hand, the electron interactions are responsible for the orbital polarization, which breaks the symmetry of the wavefunction and enhances the electron localization in the t_{2g} states. On the other hand, the phonon OPs induce the crystal distortion, which generates the structural transformation from the cubic $Fd\bar{3}m$ phase to the LT phase with monoclinic $P2_1/c$ symmetry. The coupling between these two subsystems is crucial since none of them alone would be able to explain the metal-insulator transition which occurs in magnetite at T_V . As we have shown, without the Hubbard interaction U , the EP interaction would be too weak to induce structural changes. In the presence of electron correlations, the coupling between the electrons in t_{2g} states and phonons is largely enhanced since it leads to stabilization of the OO and to lowering of the total energy. The corresponding CO is very subtle and seems to be rather a consequence of the joint effect of the OO and enhanced EP interactions than the driving force of the VT.

The splitting of the t_{2g} states due to the EP interaction is usually referred to as the Jahn-Teller effect. In principle, the mechanism observed in magnetite is similar to this effect, however, it differs in many respects from the classical examples. In a typical situation, one considers the displacements of oxygen ions around the transition metal cations, which break the symmetry and split the degenerate $3d$ states. As we discussed in the previous Sections, the displacement pattern in the monoclinic structure is more complicated and involves also $Fe(B)$ ions. In particular, in the X_3 mode the iron atoms (with largest amplitudes) vibrate in the same plane as oxygens. Therefore, the orbital polarization results in this case mainly from the interplanar interactions between iron and oxygen ions.

A dynamical coupling between the charge-orbital fluctuations and phonons induces the critical diffuse scattering above T_V . Temperature dependence of this scattering gives us important information about precursors, which show up far from the critical point. The signs of the transition appear already at about 200 K. Apart from neutron scattering coming from \mathbf{k}_F and \mathbf{k}_X points,^{43,45} there are maxima at other positions, also with an incommensurate wavelengths. For instance, very pronounced critical behavior was observed at $\mathbf{k} = (8, 0, 0.75)$.⁴² When temperature is lowered, the coupling between different modes, described by the Landau free energy (12), leads to stabilization of particular phonons with commensurate wavelengths. Very close to the transition point, about 5 K above T_V , the Δ_5 OP becomes active, producing the signal in neutron measurement.³⁹ The question arises why

is this mode observed only a few kelvins above T_V , while signals from the Γ and X points are seen at much higher temperatures? This may be connected with the relative strength of different OPs. In Fig. 2, we see that the coupling to Δ_5 mode is weaker than to X_3 mode, and it gives a different signal in neutron scattering.

Critical scattering is one of indications of a short-range (charge and orbital) order above the VT, first discussed by Anderson.³ Another evidence is connected with the change in entropy, which is smaller than in the order-disorder phase transitions.⁸⁶ Also the temperature dependence of resistivity at $T > T_V$, which is not typical for metals, suggests the polaronic nature of charge carriers. First photoemission measurements indicated the gap closing above T_V ,³² but more detailed studies^{33,34,87} established that the gap only decreases, without any sharp change at T_V . The optical conductivity studies suggest also the gap opening below T_V , but above the transition the conductivity spectrum does not exhibit a metallic Drude-type behavior.⁵⁶ Instead, a hopping type conductivity is observed, with highly diffuse character of charge dynamics. This picture is supported by the structural EXAFS studies, which found that the local crystal geometry does not change at T_V .⁵⁰ It means that the quasistatic lattice distortions are present already in the high-symmetry cubic phase above T_V . All these results are consistent with the present theory, which shows that some phonons strongly couple to electronic states and may induce local crystal deformations and polaronic short range order above T_V .

As demonstrated in this work and the previous study,⁶⁰ the theoretical approach based on the GGA+ U (or LDA+ U) provides a very good description of the VT. However, there are some aspects, which involve dynamical processes and many-body interactions. For example, the detailed analysis of the photoemission spectra showed that the DFT is not sufficient to explain changes induced by the VT and better agreement with experiment can be achieved only by using the DMFT approach.⁵⁸ An interesting effect was observed in the spin excitation spectrum, which shows a large splitting in the acoustic magnon branch at \mathbf{k}_Δ below the VT.⁸⁸ This effect cannot be explained merely by the dependence of exchange interactions on the crystal structure or charge ordering, but is rather a consequence of the magnon-phonon coupling. Additionally, a recent neutron scattering study revealed an anomalous broadening and energy shift of the Δ_5 spin wave above T_V .⁸⁹ A strong spin-phonon interaction, suggested by the present work, provides a sound starting point for studying such effects.

Finally, the behavior of magnetite at high pressure is rather intriguing. According to diffraction studies,⁹⁰ the critical temperature T_V decreases with pressure, so the VT can be induced at rather low temperature by applying pressure in the LT monoclinic phase. Recently two contradicting views on the VT based on pressure experiments have been suggested. On the one hand, a possible transition from the inverse to normal spinel structure has

been suggested as consistent with the interpretation of the Mössbauer and x-ray scattering measurements.^{91,92} This scenario precludes a CO on the Fe(*B*) sites below T_V , but predicts a large $\sim 50\%$ increase in the bulk magnetization with increasing pressure or by lowering temperature. On the other hand, no change in magnetic moments at both *A* and *B* sites has been detected by the neutron diffraction studies in a broad range of pressure up to $p = 5.3$ GPa.⁹³ This latter result rules out a possibility of the inverse spinel to normal spinel transition under decreasing temperature (increasing pressure), at least in the regime of pressure lower than 5.3 GPa. It also agrees with earlier band structure calculations,²³ and with the present mechanism of structural transition in magnetite. As the electron occupations at *A* and *B* sites are modified rather weakly, no significant change in the values of magnetic local moments is expected. We emphasize that this latter view does not imply large CO below the VT. In fact, the structural transition suggested in the present work not only *explains* the dramatic change in the conductivity observed at T_V , but also *predicts* rather weak CO, in agreement with experiment.^{18,19,20,21}

VII. SUMMARY AND CONCLUSIONS

In this work, we have presented a detailed group theory analysis of the Verwey transition. We have identified three primary OPs: X_3 , Δ_5 , and T_{2g} , which describe the symmetry reduction in the crystal structure transformation from the high-temperature cubic $Fd3m$ phase to the LT monoclinic $P2/c$ phase. By performing the numerical *ab initio* computations, we have demonstrated that a prominent role is played by the X_3 mode which: (i) couples strongly to the electronic states, (ii) lowers the total energy, and (iii) is responsible for the metal-insulator transition. The latter transition occurs only when local Coulomb interaction U is explicitly included in t_{2g} iron states and may trigger weak charge order at *B* sites. In fact, this phenomenon appears counterintuitive and occurs only as a result of the accompanying local lattice distortions which may be seen as a Jahn-Teller lattice instability. These results support the recent point of view^{60,94} that neither pure electrostatics is the main factor responsible for the charge order observed below the Verwey transition, nor the charge order is the mechanism driving the transition by itself. At the same time, the local Coulomb interaction generates alternating orbital order, which leads to strong reduction of charge mobility

and amplifies electron-lattice effects.

The present study reconciles several previous points of view on the Verwey transition in magnetite and suggests that the physical effects which occur simultaneously below this transition in the monoclinic $P2/c$ phase can be classified into the ones which are the primary cause of the symmetry change and the ones which occur only as its consequence. In this way it contributes to the recent debate concerning the origin of the transition and clarifies the role played in it by the charge order. While weak charge order has been found at Fe(*B*) sites, it is not surprising that it does not obey the Verwey model. In fact, it is only one of the manifestations of strong local electron interactions in partly occupied t_{2g} states rather than the primary cause of the observed symmetry change.

We have also compared phonon energy spectrum of magnetite with the experimental data obtained by Raman and infrared spectroscopy, as well as by neutron scattering. We have found that phonon frequencies strongly depend on local electron interactions, and the GGA+ U calculations performed with realistic parameters for Fe ions ($U = 4.0$ eV and $J = 0.8$ eV) give very satisfactory qualitative and quantitative agreement with the experimental data. In contrast, when the electron interaction effects are neglected, the phonon spectra are even qualitatively different from the observed ones.

Summarizing, we have shown that the Verwey transition is promoted by a set of order parameters with mixed electron and phonon character. The insulating monoclinic $P2/c$ phase occurs below the transition as a result of the instability driven by the electron-phonon coupling in presence of strong electron correlations. We argue that the electron-lattice coupling plays an important role also in other transition metal oxides with strongly correlated electrons. Further studies of the lattice relaxation effects in these systems may lead to discoveries of new electronic phenomena that could be understood only by simultaneous treatment of electronic and lattice degrees of freedom.

Acknowledgments

The authors thank A. Kozłowski, J. Łażewski, and P.T. Jochym for valuable discussions. This work was partially supported by Marie Curie Research Training Network under Contract No. MRTN-CT-2006-035957 (c2c). A. M. Oleś would like to acknowledge support by the Polish Ministry of Science and Education under Project No. N202 068 32/1481.

¹ E. J. W. Verwey, *Nature* (London) **144**, 327 (1939).

² E. J. W. Verwey and P. W. Haayman, *Physica* (Amsterdam) **9**, 979 (1941).

³ P. W. Anderson, *Phys. Rev.* **102**, 1008 (1956).

⁴ F. Walz, *J. Phys.: Condens. Matter* **14**, R285 (2002).

⁵ M. Imada, A. Fujimori, and Y. Tokura, *Rev. Mod. Phys.*

70, 1039 (1998).

⁶ E. J. Samuelsen, E. J. Bleeker, L. Dobrzynski, and T. Riste, *J. Appl. Phys.* **39**, 1114 (1968); T. Yamada, K. Suzuki, S. Chikazumi, *Appl. Phys. Lett.* **13**, 172 (1968).

⁷ M. Iizumi and G. Shirane, *Solid State Commun.* **17**, 433 (1975).

- ⁸ M. Iizumi, T. F. Koetzle, G. Shirane, S. Chikazumi, M. Matsui, and S. Todo, *Acta Crystallogr., Sect. B* **B38**, 2121 (1982).
- ⁹ J. Yoshida and S. Iida, *J. Phys. Soc. Jpn.* **42**, 230 (1977).
- ¹⁰ J. M. Zuo, J. C. Spence, and W. Petuskey, *Phys. Rev. B* **42**, 8451 (1990).
- ¹¹ M. Mizoguchi, *J. Phys. Soc. Jpn.* **44**, 1501 (1978).
- ¹² P. Novak, H. Stepankova, J. Englich, J. Kohout, and V. A. M. Brabers, *Phys. Rev. B* **61**, 1256 (2000).
- ¹³ M. Mizoguchi, *J. Phys. Soc. Jpn.* **70**, 2333 (2001).
- ¹⁴ J. P. Wright, J. P. Attfield, and P. G. Radaelli, *Phys. Rev. Lett.* **87**, 266401 (2001).
- ¹⁵ J. P. Wright, J. P. Attfield, and P. G. Radaelli, *Phys. Rev. B* **66**, 214422 (2002).
- ¹⁶ J. Garcia, G. Subias, M. G. Proietti, J. Blasco, H. Renevier, J. L. Hodeau, and Y. Joly, *Phys. Rev. B* **63**, 054110 (2001).
- ¹⁷ G. Subias, J. Garcia, J. Blasco, M. G. Proietti, H. Renevier, and M. C. Sanchez, *Phys. Rev. Lett.* **93**, 156408 (2004).
- ¹⁸ R. J. Goff, J. P. Wright, J. P. Attfield, and P. G. Radaelli, *J. Phys.: Condens. Matter* **17**, 7633 (2005).
- ¹⁹ D. J. Huang, H.-J. Lin, J. Okamoto, K. S. Chao, H.-T. Jeng, G. Y. Guo, C.-H. Hsu, C.-M. Huang, D. C. Ling, W. B. Wu, C. S. Yang, and C. T. Chen, *Phys. Rev. Lett.* **96**, 096401 (2006).
- ²⁰ E. Nazarenko, J. E. Lorenzo, Y. Joly, J. L. Hodeau, D. Mannix, and C. Martin, *Phys. Rev. Lett.* **97**, 056403 (2006).
- ²¹ J. Schlappa, C. Schübler-Langeheine, C. F. Chang, H. Ott, A. Tanaka, Z. Hu, M. W. Haverkort, E. Schierle, E. Wschke, G. Kaindl, and L. H. Tjeng, *cond-mat/0605096* (unpublished).
- ²² A. Yanase and K. Siratori, *J. Phys. Soc. Jap.* **53**, 312 (1984).
- ²³ Z. Zhang and S. Satpathy, *Phys. Rev. B* **44**, 13319 (1991).
- ²⁴ A. Yanase and N. Hamada, *J. Phys. Soc. Jpn.* **68**, 1607 (1999).
- ²⁵ V. I. Anisimov, I. S. Elfimov, N. Hamada, and K. Terakura, *Phys. Rev. B* **54**, 4387 (1996).
- ²⁶ V. N. Antonov, B. N. Harmon, V. P. Antropov, A. Y. Perlov, and A. N. Yaresko, *Phys. Rev. B* **64**, 134410 (2001).
- ²⁷ Z. Szotek, W. M. Temmermann, A. Svane, L. Petit, G. M. Stocks, and H. Winter, *Phys. Rev. B* **68**, 054415 (2003).
- ²⁸ G. K. H. Madsen and P. Novak, *Europhys. Lett.* **69**, 777 (2005).
- ²⁹ I. Leonov, A. N. Yaresko, V. N. Antonov, M. A. Korotin, and V. I. Anisimov, *Phys. Rev. Lett.* **93**, 146404 (2004).
- ³⁰ H.-T. Jeng, G. Y. Guo, and D. J. Huang, *Phys. Rev. Lett.* **93**, 156403 (2004).
- ³¹ J. R. Neal, A. J. Behan, A. Mokhtari, M. R. Ahmed, H. J. Blythe, A. M. Fox, and G. A. Gehring, *J. Magn. Magn. Mater.* **310**, e246 (2007).
- ³² A. Chainani, T. Yokoya, T. Morimoto, T. Takahashi, and S. Todo, *Phys. Rev. B* **51**, 17976 (1995).
- ³³ J.-H. Park, L. H. Tjeng, J. W. Allen, P. Metcalf, and C. T. Chen, *Phys. Rev. B* **55**, 12813 (1997).
- ³⁴ D. Schrupp, M. Sing, M. Tsunekawa, H. Fujiwara, S. Kasai, A. Sekiyama, S. Suga, T. Muro, V. A. M. Brabers, and R. Claessen, *Europhys. Lett.* **70**, 789 (2005).
- ³⁵ T. J. Moran and B. Lüthi, *Phys. Rev.* **187**, 710 (1969).
- ³⁶ H. Shwenk, S. Bareiter, C. Hinkel, B. Lüthi, Z. Kakol, A. Kozłowski, and J. M. Honig, *Eur. Phys. J. B* **13**, 491 (2000).
- ³⁷ M. M. Seikh, C. Narayana, P. A. Metcalf, J. M. Honig, and A. K. Sood, *Phys. Rev. B* **71**, 174106 (2005).
- ³⁸ E. J. Samuelsen and O. Steinsvoll, *Phys. Status Solidi B* **61**, 615 (1974).
- ³⁹ Y. Fujii, G. Shirane, and Y. Yamada, *Phys. Rev. B* **11**, 2036 (1975).
- ⁴⁰ Y. Yamada, *AIP Conf. Proc.* **24**, 79 (1974).
- ⁴¹ K. Chiba, K. Suzuki, and S. Chikazumi, *J. Phys. Soc. Jpn.* **39**, 839 (1975).
- ⁴² S. M. Shapiro, M. Iizumi, and G. Shirane, *Phys. Rev. B* **14**, 200 (1976).
- ⁴³ Y. Yamada, N. Wakabashi, and R. M. Nicklow, *Phys. Rev. B* **21**, 4642 (1980).
- ⁴⁴ Y. Yamada, *Phil. Mag. B* **42**, 377 (1980).
- ⁴⁵ K. Siratori, Y. Ishii, Y. Morii, S. Funahashi, S. Todo, and A. Yanase, *J. Phys. Soc. Jpn.* **67**, 2818 (1998).
- ⁴⁶ E. I. Terukov, W. Reichelt, D. Ihle, and H. Oppermann, *Phys. Status Solidi B* **95**, 491 (1979).
- ⁴⁷ L. Degiorgi, I. Blatter-Mörke, and P. Wachter, *Phys. Rev. B* **35**, 5421 (1987).
- ⁴⁸ L. V. Gasparov, D. B. Tanner, D. B. Romero, H. Berger, G. Margaritondo, and L. Forro, *Phys. Rev. B* **62**, 7939 (2000).
- ⁴⁹ R. Gupta, A. K. Sood, P. Metcalf, and J. M. Honig, *Phys. Rev. B* **65**, 104430 (2002).
- ⁵⁰ G. Subias, J. Garcia, and J. Blasco, *Phys. Rev. B* **71**, 155103 (2005).
- ⁵¹ B. Handke, A. Kozłowski, K. Parlinski, J. Przewoznik, T. Slezak, A. I. Chumakov, L. Niesen, Z. Kakol, and J. Korecki, *Phys. Rev. B* **71**, 144301 (2005).
- ⁵² D. Ihle and B. Lorenz, *Phys. Status Solidi B* **96**, 659 (1979).
- ⁵³ J. R. Cullen and E. R. Callen, *J. Appl. Phys.* **41**, 879 (1970); *Phys. Rev. B* **7**, 397 (1973).
- ⁵⁴ D. Ihle and B. Lorenz, *Phil. Mag. B* **42**, 337 (1980).
- ⁵⁵ D. Ihle and B. Lorenz, *J. Phys. C: Solid State Phys.* **19**, 5239 (1986).
- ⁵⁶ S. K. Park, T. Ishikawa, and Y. Tokura, *Phys. Rev. B* **58**, 3717 (1998).
- ⁵⁷ H. Seo, M. Ogata, and H. Fukuyama, *Phys. Rev. B* **65**, 085107 (2002).
- ⁵⁸ L. Craco, M. S. Laad, and E. Müller-Hartmann, *Phys. Rev. B* **74**, 064425 (2006).
- ⁵⁹ H. P. Pinto and S. D. Elliott, *J. Phys.: Condens. Matter* **18**, 10427 (2006).
- ⁶⁰ P. Piekarczyk, K. Parlinski, and A. M. Oleś, *Phys. Rev. Lett.* **97**, 156402 (2006).
- ⁶¹ K. Parlinski, Z. Q. Li, and Y. Kawazoe, *Phys. Rev. Lett.* **78**, 4063 (1997).
- ⁶² O. V. Kovalev, *Representations of the Crystallographic Space Groups*, 2nd ed. (Gordon and Breach, New York, 1993).
- ⁶³ K. Parlinski, *Z. Phys. B* **58**, 245 (1985).
- ⁶⁴ D. Hatch and H. Stokes, *Phys. Rev. B* **65**, 014113 (2001).
- ⁶⁵ K. Parlinski and M. Parlinska-Wojtan, *Phys. Rev. B* **66**, 064307 (2002).
- ⁶⁶ H. T. Stokes and D. M. Hatch, COPL software (2001); www.physics.byu.edu/stokesh/isotropy.html.
- ⁶⁷ H. T. Stokes and D. M. Hatch, ISOTROPY software (2002); stokes.byu.edu/isotropy.html.
- ⁶⁸ J. Yoshida and S. Iida, *J. Phys. Soc. Jpn.* **47**, 1627 (1979).
- ⁶⁹ M. Iizumi, *AIP Conf. Proc.* **53**, 184 (1979).
- ⁷⁰ G. Kresse and J. Furthmüller, *Comput. Mater. Sci.* **6**, 15 (1996).

- ⁷¹ J. P. Perdew, J. A. Chevary, S. H. Vosko, K. A. Jackson, M. R. Pedersen, D. J. Singh, and C. Fiolhais, *Phys. Rev. B* **46**, 6671 (1992).
- ⁷² P. E. Blöchl, *Phys. Rev. B* **50**, 17953 (1994).
- ⁷³ G. Kresse and J. Joubert, *Phys. Rev. B* **59**, 1758 (1999).
- ⁷⁴ H. J. Monkhorst and J. D. Pack, *Phys. Rev. B* **13**, 5188 (1976).
- ⁷⁵ J. Łażewski, P. Piekarczyk, A. M. Oleś, and K. Parlinski, *Phys. Rev. B* **74**, 174304 (2006).
- ⁷⁶ J. Zaanen and G. A. Sawatzky, *J. Solid State Chem.* **88**, 8 (1990).
- ⁷⁷ Thereby we neglect the anisotropy of Hund's exchange which varies for pairs of $3d$ electrons between C and $4B+C$, see, e.g. A. M. Oleś, G. Khaliullin, P. Horsch, and L. F. Feiner, *Phys. Rev. B* **72**, 214431 (2005).
- ⁷⁸ A. I. Liechtenstein, V. I. Anisimov, and J. Zaanen, *Phys. Rev. B* **52**, R5467 (1995).
- ⁷⁹ I. Leonov, A. N. Yaresko, V. N. Antonov, and V. I. Anisimov, *Phys. Rev. B* **74**, 165117 (2006).
- ⁸⁰ K. Parlinski, Software PHONON, Cracow, 2005.
- ⁸¹ V. C. Rakcecha and N. S. Satya Murthy, *J. Phys. C* **11**, 4389 (1978).
- ⁸² R. Aragon, *Phys. Rev. B* **46**, 5328 (1992).
- ⁸³ P. Novak, J. Kunes, and P. M. Oppeneer, *Physica B* **312-313**, 785 (2002).
- ⁸⁴ H.-T. Jeng, G. Y. Guo, and D. J. Huang, *Phys. Rev. B* **74**, 195115 (2006).
- ⁸⁵ J. Garcia, G. Subias, M. G. Proietti, H. Renevier, Y. Joly, J. L. Hodeau, J. Blasco, M. C. Sanchez, and J. F. Berar, *Phys. Rev. Lett.* **85**, 578 (2000).
- ⁸⁶ J. P. Sheperd, J. W. Koenitzer, R. Aragon, J. Spalek, and J. M. Honig, *Phys. Rev. B* **43**, 8461 (1991).
- ⁸⁷ E. Goering, S. Gold, M. Lafkioti, G. Schütz, and V. A. M. Brabers, *Phys. Rev. B* **72**, 033112 (2005).
- ⁸⁸ R. J. McQueeney, M. Yethiraj, W. Montfrooij, J. S. Gardner, P. Metcalf, and J. M. Honig, *Phys. Rev. B* **73**, 174409 (2006);
- ⁸⁹ R. J. McQueeney, M. Yethiraj, S. Chang, W. Montfrooij, T. G. Perring, J. M. Honig, and P. Metcalf, arXiv:0707.2253 (unpublished).
- ⁹⁰ G. K. Rozenberg, M. P. Pasternak, W. M. Xu, Y. Amiel, M. Hanfland, M. Amboage, R. D. Taylor, and R. Jeanloz, *Phys. Rev. Lett.* **96**, 045705 (2006).
- ⁹¹ M. P. Pasternak, W. M. Xu, G. Kh. Rozenberg, R. D. Taylor, and R. Jeanloz, *J. Magn. Magn. Mater.* **265**, L107 (2003).
- ⁹² G. Kh. Rozenberg, Y. Amiel, W. M. Xu, M. P. Pasternak, R. Jeanloz, M. Hanfland, and R. D. Taylor, *Phys. Rev. B* **75**, 020102 (2007).
- ⁹³ S. Klotz, G. Rousse, Th. Strässle, C. L. Bull, and M. Guthrie, *Phys. Rev. B* **74**, 012410 (2006).
- ⁹⁴ I. Leonov and A. N. Yaresko, *J. Phys.: Condens. Matter* **19**, 021001 (2007).